Geotech Geol Eng (2023) 41:927–942
https://doi.org/10.1007/s10706-022-02315-2

ORIGINAL PAPER

Exploratory Seepage Detection in a Laboratory-Scale Earthen Dam Based on Distributed Temperature Sensing Method

Binyam Bekele · Chung Song · Jongwan Eun · Seunghee Kim

Received: 16 March 2022 / Accepted: 2 October 2022 / Published online: 14 October 2022

Abstract The hydro-thermal coupled seepage condition assessment based on the fiber optic Distributed Temperature Sensing (DTS) is becoming popular, particularly in field-scale dams, due to DTS's capability to provide spatially continuous temperature data. However, there is limited research examining this DTS's capability in laboratory-scale dams due to the practical challenge of spatial resolution of the sensor. This study demonstrated and evaluated the applicability of spirally wound custom DTS in a laboratory-scale dam. By varying the reservoir water temperature, the DTS's capability in capturing dam's internal spatiotemporal temperature variations and detecting the seepage patterns was investigated. Thermal camera imaging and numerical modeling were additionally implemented to support and verify the laboratory findings. It was found that the DTS effectively captured the elevation-wise variability of temperature, seepage, and the location of phreatic line in the model dam. It was also observed that DTS may not necessarily reflect seepage conditions at the sensing location. Instead, it may provide general information about seepage conditions upstream of the sensing location.

Keywords Distributed temperature sensing · Spatial resolution · Hydro-thermal coupling · Laboratory-scale dam · Seepage detection

B. Bekele (✉) · C. Song · J. Eun · S. Kim
Department of Civil and Environmental Engineering, University of Nebraska-Lincoln, Lincoln, NE, USA
e-mail: bbekele@huskers.unl.edu

C. Song
e-mail: csong8@unl.edu

J. Eun
e-mail: jeun2@unl.edu

S. Kim
e-mail: seunghee.kim@unl.edu

1 Introduction

Earth dams provide many benefits to humans, such as electricity, irrigation water, flood control, recreation spaces, etc. However, seepage-related issues arising from material susceptibility, abnormal stress conditions, and extreme hydraulic gradient may pose significant concerns to their safety (Garner and Fannin 2010; USBR 2014). Perhaps, seepage-related problems are one of the leading failure modes in earth dams (Fell et al. 2003; Foster et al. 2000; Fry 2016; Robbins and Griffiths 2018). According to the history of dam failures, they account about 50% of dam failure worldwide (Fell and Fry 2007; Foster et al. 2000; Fry 2016; Robbins and Griffiths 2018; Torres 2009) and about 20% of dam failures in the U.S. (ASDSO 2022). Therefore, reliable seepage monitoring approach is important to ensure safe operation of dams (FEMA 2015; Goltz 2011; Johansson 1997; Mattsson et al. 2008; USBR 2014).

The hydro-thermal coupled approach is one of the newly emerged seepage monitoring methods (Bersan et al. 2019; Dornstädter 1996; Dornstädter et al. 2017). The technique assumes that heat carried by seepage flow creates temperature changes in a dam body through mechanisms of heat conduction and advection. Under slow seepage conditions, the temperature change is primarily governed by conduction. However, under concentrated seepage, the soil temperature is additionally affected by advection (bulk transport of heat by water) (Johansson 1997), leading to a temperature anomaly in the dam. Thus, with the deployment of a temperature sensing tool, locations of these thermal anomalies indicating a potential seepage issue may be identified.

In recent years, fiber optics Distributed Temperature Sensing (DTS) has become a popular means for dam thermal monitoring due to its unmatched spatial coverage compared to conventional point-wise sensors, with temperature data as low as 0.25 m intervals for tens of kilometers stretch (Fabritius et al. 2017). In addition, its low operational cost, durability, and temporal coverage have been favorable for long-term seepage assessment (Des Tombe et al. 2020; Glisic and Inaudi 2008; Inaudi and Glisic 2007; Loupos and Amditis 2017; Soga et al. 2015, 2019).

In the past, several researchers have used DTS for temperature-based assessment of seepage through field-scale dams (Belli and Inaudi 2017; Bersan et al. 2019; Cola et al. 2021; Dornstädter et al. 2017) because the spatial resolution of DTS, which is typically 1 m, is usually comfortable for large-scale uses, and the technique is cost-effective. Despite being few, laboratory-scale tests and computational studies have been also conducted to evaluate the feasibility of using DTS in the laboratory (Ghafoori et al. 2020a) and to prove the capability of DTS for seepage monitoring (Song and Yosef 2017). However, there is limited research in realizing the full capability of DTS in capturing the temperature-seepage interaction in a well-controlled laboratory-scale earth dam. The practical challenge in laboratory research is the limited space to accommodate DTS's spatial resolution. Therefore, previous laboratory-based studies were able to measure sparse temperature readings similar to point-wise temperature sensors (Ghafoori et al. 2020a; Xiao and Huang 2013).

This study demonstrated and evaluated the capability of a spirally wound custom fabricated DTS to capture high-resolution temperature and seepage patterns in a laboratory-scale earth dam model. After winding the DTS cable around a PVC pipe, the original spatial resolution of 1 m was enhanced to 8.5 mm. This DTS was installed at the model dam's center and the dam was subjected to variable reservoir temperatures and a hydraulic head. The subsequent internal temperature variation was captured by the DTS. Then, the spatiotemporal temperature distribution and temperature–time lag behavior obtained from the DTS were analyzed to evaluate the seepage through the dam. In addition, thermal camera imaging and calibrated hydro-thermal coupled computational study were conducted to support the laboratory study and verify the capability of the adopted approach in detecting reliable temperature and seepage conditions of the dam.

2 Characteristics of the DTS

2.1 Interrogator and Fiber Optic Cable

The interrogator is a device that sends, receives, and evaluates a laser light pulse through the fiber optic cable (Des Tombe et al. 2020; Hartog 2017). The interrogator used in this study (LIOS PRE.VENT DSM) has four channels, each having a distance range of up to 5000 m. It can deliver temperature information at a minimum sampling resolution of 0.25 m and a maximum spatial resolution of 1 m. Its temperature resolution is 0.01 °C. The measurement time was approximately 1 min in this study. However, measurement time may increase for longer DTS cables.

A single-mode optical fiber cable (SMF-28-100) with a 1260–1625 nm operating wavelength was deployed. The fiber's core and cladding are 8.2 and 125 µm, respectively. The total diameter of the fiber, including the outer jacket, is 900 µm. The operating temperature of the fiber is from −60 °C to 85 °C. Under an ideal condition, the expected total attenuation of the fiber (absorption and scattering) is less than 0.18 dB/km at 1550 nm operating wavelength. The bend loss is less than 0.01 dB for 100 turns on a 2.5 cm mandrel per the manufacturer's specification.

The temperature is evaluated based on the Brillouin scattering principle. The frequency shift due to strain and temperature is computed, as shown below (Hartog 2017; Maughan et al. 2001),

$$\Delta v_B = C_{v_B E}\Delta\varepsilon + C_{v_B T}\Delta T \quad (1)$$

where, Δv_B is the Brillouin frequency shift; $\Delta\varepsilon$ is the change in strain;ΔT is the change in temperature; $C_{v_B E}$, and $C_{v_B T}$ are the strain and temperature coefficients, respectively that depend on the type of fiber and operating wavelength. The temperature can be obtained directly from the frequency shift if the fiber is free from strain. However, the frequency shift due to strain should be accounted for if the fiber is subjected to strain.

2.2 Enhancing the Spatial Resolution

The inherent spatial resolution, i.e., 1 m, was enhanced to achieve the full potential of DTS in the laboratory-scale model dam. As such, a custom DTS was made by wrapping the fiber optic cable around a PVC pipe of a 3.34 cm outer diameter, as shown in Fig. 1a. The enhancement was governed mainly by the winding circumference and fiber thickness, as shown in Eq. (2). Similar technique has been implemented by other researches in different field of study (Briggs et al. 2012; Sarabia et al. 2018; Suárez et al. 2011; Wu et al. 2020).

$$R_{imp} = \frac{R_{sys}}{\pi D_{PVC}} D_{Jacket} \quad (2)$$

where, R_{imp} is the improved (new) spatial resolution; R_{sys} is the inherent spatial resolution of the system, which was 1 m in this study; D_{PVC} is the diameter of the PVC (3.34 cm), and D_{Jacket} is the overall thickness of the fiber (900 µm). Increasing the diameter of the PVC will enhance the spatial resolution along the winding direction.

After plugging all quantities in Eq. (2), the improved spatial resolution approximately became 8.5 mm, as shown in Fig. 1a. However, it is noted that sampling data points may not be arranged in a straight line because 1 m of the fiber divided by the circumference of the pipe did not compute a whole number.

The effect of the winding was evaluated by comparing the light attenuation before and after winding. Figure 1b shows the backscattered light level before and after winding. Due to winding, there was a 0.33 dB loss for 100 m of the fiber optic cable. This loss was 1.83 times the manufacturer's rated loss for 1 km of fiber optic cable (i.e., 0.18 dB/km) without winding. Therefore, the extra loss induced was noted to be the result of the macro-bending of the fiber during winding.

2.3 Calibration for the Effect of Pre-Existing Strain

The winding induced pre-straining in the fiber, which in turn generated a Brillouin frequency shift in the light [see Eq. (1)]. Therefore, calibration was performed to compensate for the influence of pre-straining in the DTS readings. To perform the calibration, first, the wound fiber optic cable was immersed in water with a known temperature. Then, the DTS readings at various times were matched with measured temperature (from a thermometer) to obtain an appropriate calibration factor, as shown in Eq. (3):

$$\min_{C_t}\left[\sum (T_{DTS} - T_m)^2\right] = \min_{C_t}\left[\sum (T_i + C_t \times \Delta T_{DTS} - T_m)\right] \quad (3)$$

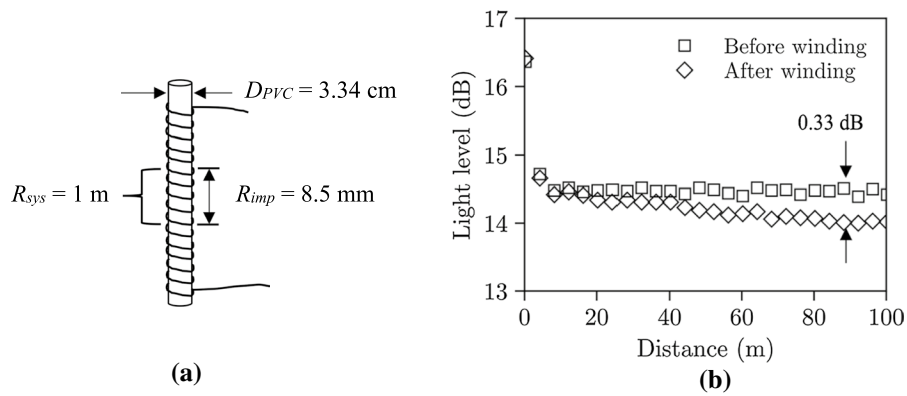

Fig. 1 **a** DTS wound around 3.34 cm diameter PVC pipe, and **b** Backscattered light level before and after winding

where, min[ ] is minimization of the function inside the square bracket; C_t is the calibration parameter; T_{DTS} is the absolute temperature reading by the DTS and is given by $T_{DTS} = T_i + C_t \Delta T_{DTS}$; T_i is the reference temperature = 21.5 °C (during calibration); ΔT_{DTS} is the differential temperature from the DTS, and T_m is the absolute temperature obtained from the thermometer. C_t turns out to be 0.55 after optimization of the equation. That means raw DTS data is reduced by 45% to account for the pre-straining effect induced during winding.

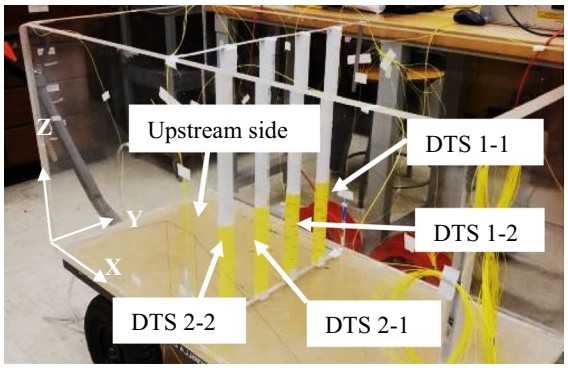

Fig. 3 Vertically installed high-resolution DTS at the middle of the acrylic box

3 Laboratory Modeling

3.1 Description of the Model

The laboratory model earth dam was constructed in a clear acrylic box as shown in Fig. 2. The box had inside dimensions of length x width x height = 117 cm × 56 cm × 58 cm, with panel thickness of 2.54 cm. The dam had 27 cm height, 9.5 cm top width, and 117 cm bottom width. The transverse width was 56 cm, equal to the inside width of the box. The maximum upstream and downstream water heads were 22.5 cm and 6 cm, respectively.

Four vertical DTS systems (DTS 1–1, 1–2, 2–1, and 2–2) were installed in the middle of the dam, as shown in Figs. 2 and 3. The DTSs were installed vertically following a similar technique adopted by previous researchers (Dornstädter 2013; Dornstädter et al. 2017; Fabritius et al. 2017). Multiple DTSs were established to investigate repeatability and seepage patterns across a plane through the dam axis. The horizontal center-to-center spacing between the DTSs was 11.2 cm, while the total sensing height was 24 cm (direction Z) from the bottom of the dam.

The dam material was a poorly graded sand, with the gradation shown in Fig. 4a (ASTM International D2487 2020). It has negligible fine particles (percent finer than #200 sieve = 0.13%). From a density test and a constant head permeability test (ASTM International D2434 2019), the dry density and hydraulic conductivity were determined to be 1.784 g/cm^3 and 3.4×10^{-4} m/s, respectively. The higher hydraulic conductivity ensured fast seepage and reduced testing time. To protect the sand from possible erosion, riprap was placed on the upstream and downstream faces of the dam, as shown in Fig. 4b.

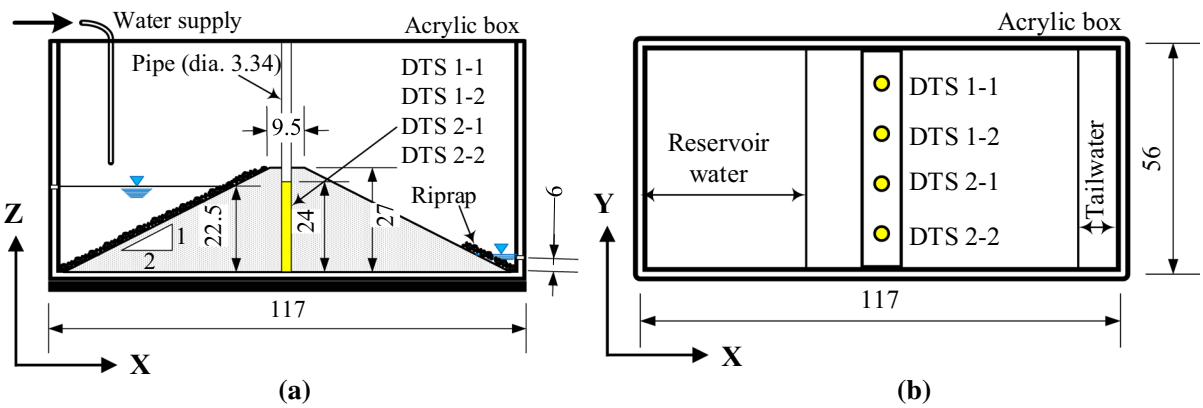

Fig. 2 **a** The laboratory model layout *Note*: all units are in cm, and **b** top of the layout

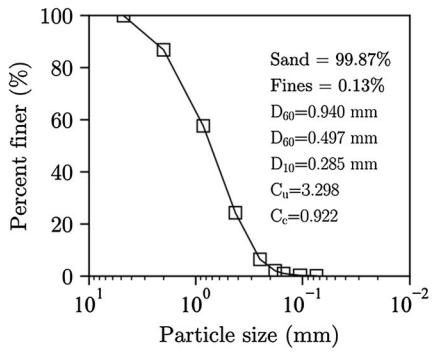

(a)

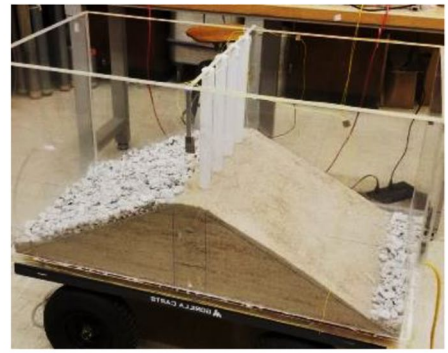

(b)

Fig. 4 **a** Gradation curve of the sand and **b** the complete dam *Note*: D_{60}, D_{30}, and D_{10} are particle sizes corresponding to 60%, 30%, and 10% finer, respectively. C_u and C_c are coefficients of uniformity and curvature, respectively

3.2 Test Procedure

Before testing, the reservoir was filled with water to the designated level and maintained for a few hours until the dam was fully wet, as shown in Fig. 5a and b. Then, resting time was applied to stabilize the internal temperature. During the test, the reservoir level gradually increased to a maximum level of 22.5 cm in 20 min and then kept constant throughout the experiment. The reservoir temperature was varied to mimic seasonal warm-cool temperature cycles, as shown in Fig. 5(c). Tap water was used as a source, and the temperature was maintained by the hot/cold valve on the tap. There were 4 phases, with two cooling and two warming phases. The phases lasted 63 min, 59 min, 64 min, and 114 min, from phase-1 (P-1) to phase-4 (P-4), respectively, as shown in Fig. 5c. The total duration of the test was 300 min. The average ambient room (air) temperature was 22.5 °C at the time of testing.

(a)

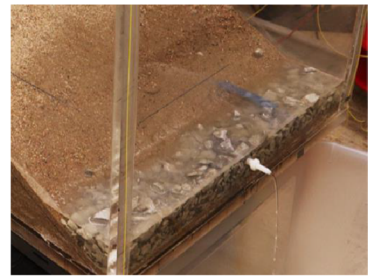

(b)

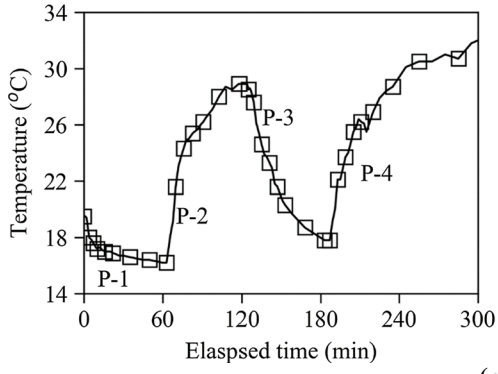

(c)

Phase	Temperature cycle	Duration (min)
P-1	Cooling (C)	63
P-2	Warming (W)	59
P-3	Cooling (C)	64
P-4	Warming (W)	114

Fig. 5 **a** scene of upstream, **b** scene of downstream, and **c** fluctuation of the reservoir temperature (measured by a thermometer) and a corresponding table showing the temperature cycles and duration of loading

3.3 Test Results

3.3.1 3 3.3. Temperature Distribution

Figure 6 shows the spatiotemporal distribution of soil temperature measured by each DTS. The x-axis is time (1-min interval), and the y-axis is the DTS position (data sampled for every 6 cm from the bottom of the box). The reservoir cooling/warming phases were superimposed on the top of the contours alongside their labels.

All DTSs installed along the dam centerline reflected the alternating reservoir temperature. However, a reduction in intensity and time lag was noticed due to the redistribution of heat and travel time to the dam's center. This result generally showed that the temporal resolution of the adopted high-resolution DTS was adequate and successful to capture the alternating reservoir temperature. In addition, a similar temporal temperature pattern in all DTSs suggested a homogenous thermal propagation across the dam centerline.

In addition, the temperature distribution showed elevation-wise variability across the DTS sensing locations. In all cases, the thermal propagation was slower in lower DTS positions, suggesting potential seepage contrast between lower and higher elevations of the dam. However, above 19 cm elevation (shown by the horizontal dashed line in the figure), the thermal propagation seems to become slower compared to just below that line. This line is believed to represent the location of the phreatic line of the dam, as discussed below.

3.3.2 Phreatic Line

The phreatic line (the line separating saturated and unsaturated flow) is a potential indicator of the seepage condition of the earth dams (Yosef and Song 2015). As such, the phreatic line of the dam was predicted from the vertical temperature profiles at different lap times, as shown in Fig. 7. The phreatic surface was identified to be around 19 cm elevation at the center of the dam based on

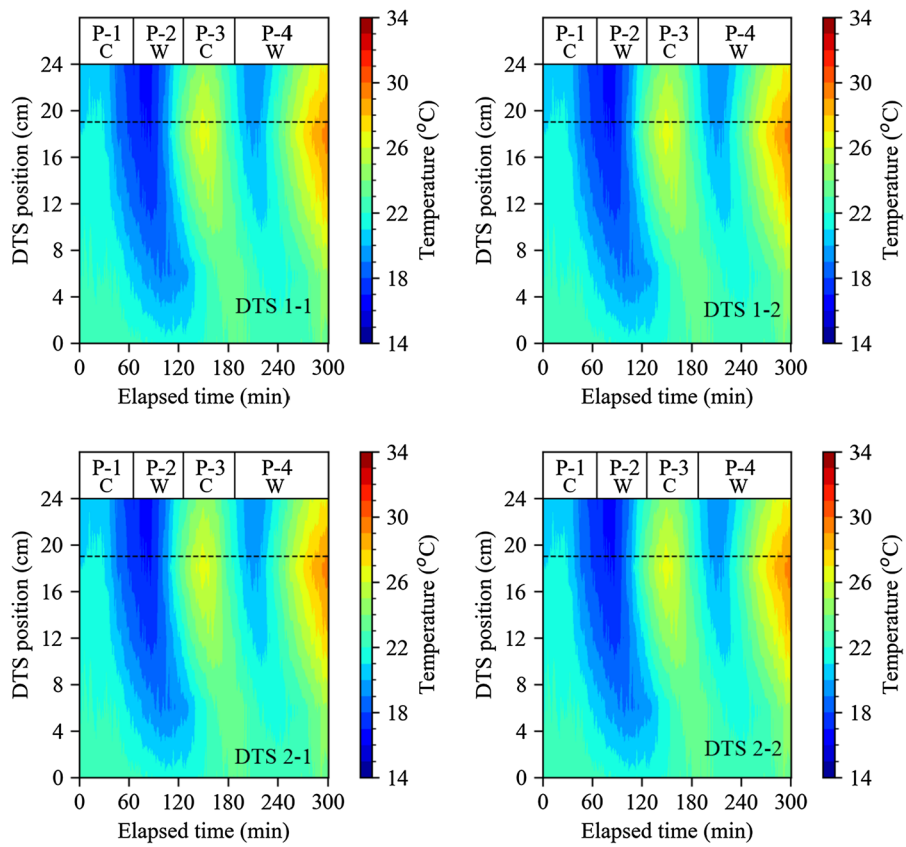

Fig. 6 Spatiotemporal distribution of temperature measured by DTS

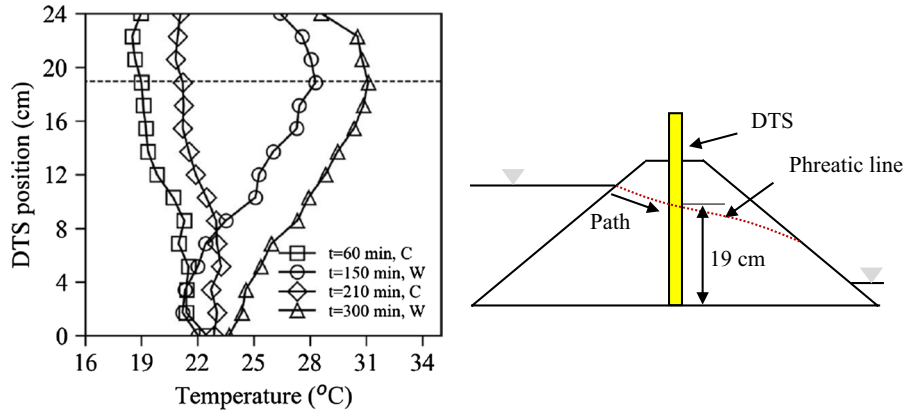

Fig. 7 Vertical temperature profiles and schematics showing the location of the potential phreatic line

the temperature profiles of the warming phases (t = 150 min, t = 300 min). Above this line, the temperature change was less due to unsaturated flow regime. The temperature at the potential phreatic line was higher than any other DTS position, indicating reduced dissipation of warm reservoir temperature. This response may be attributed to a shorter seepage path and faster seepage along the surface of the seeping water, as shown in the conceptual schematics in Fig. 7.

However, the phreatic line was not identified clearly during cooling phases (t = 60 min, t = 210 min). This behavior may be because the cooling phases (P-1 and P-3) peaks were not distinctly different from the room temperature (dam temperature near the crest) to cause noticeable inflection at the phreatic line. This observation showed the limitation of the thermal method as it needs temperature contrast between the soil and water temperature to trace seepage through the dam.

3.3.3 Time Lag and Temperature Amplitudes

A temperature time lag is induced due to the time needed for heat to travel from the source to the 'destination' (measurement location). It is affected by the distance and seepage conditions. Thus, it can be taken as an indicator of seepage conditions in a dam (Johansson 1997). As an illustration, Fig. 8 superimposes the temperature patterns at 6 cm and 18 cm elevations with the reservoir temperature to evaluate the time lag. Temperature patterns at both elevations showed a time lag. But DTS response at 6 cm elevation showed more time lag than the 18 cm elevation. That means the heat propagation needed a longer time to arrive at 6 cm elevation than 18 cm elevation. This result implied that there may be a slower seepage at 6 cm than 18 cm elevation. However, it is also expected that the heat travels a longer distance at 6 cm elevation than 18 cm elevation due to the shape of the dam widening at the lower elevations.

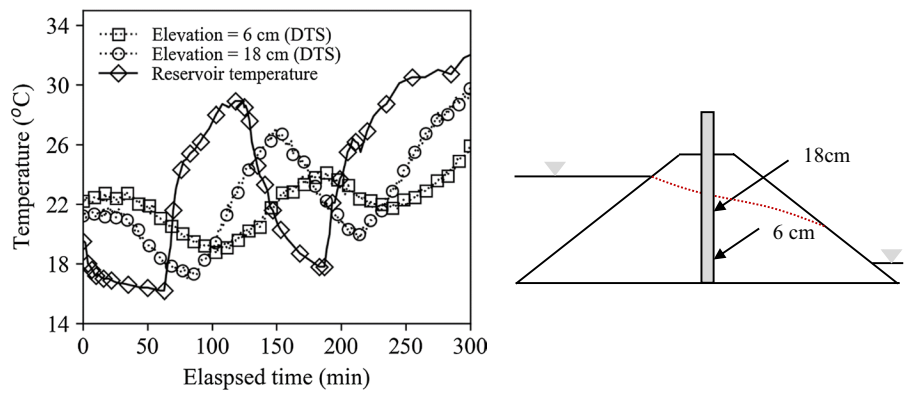

Fig. 8 Temperature time-series at 6 cm and 18 cm elevations compared with reservoir temperature fluctuation

Moreover, the input (the reservoir in this case) temperature magnitude (amplitude) reduces as it travels from the source to the sensing point due to the dissipation of heat. The travel distance and seepage conditions influence this reduction. Thus, the heat intensity is also an indicator of seepage condition (Johansson 1997). Figure 8 also shows that DTS at 6 cm elevation showed more heat damping than 18 cm elevation. This result is in line with expected heat loss over long-distance travel. It could also potentially imply a slower seepage speed through 6 cm elevation than through 18 cm elevation.

4 Thermal Images

Temperature findings from the DTS were verified with thermal images of the dam. A FLIR ONE Pro infrared thermal imaging camera was used to investigate the heat propagation along the dam. The thermal resolution of the camera is 160 × 120 pixels, its object temperature range is − 20 °C to 120 °C, and its accuracy is ± 3 °C. Figure 9a and b shows a sample thermal image captured during P-1 and P-2. Since the temperature values were found inaccurate, presumably due to the interference of the acrylic box, they are not presented to avoid misleading readers. Instead, it is noted that yellow color represented warmer temperature while purple color represented cooler temperature.

The cooler reservoir temperature from P-1 showed more tendency to propagate in a higher elevation than at lower dam elevations, as shown in the figure. The same behavior was observed during the next warming phase, P-2. These observations from the thermal images were generally aligned with the DTS results shown in Figs. 6, 7, and 8, in which, it was observed that the heat propagated faster in higher elevations and slower in lower elevations.

5 Numerical Modeling

The laboratory model demonstrated the high-resolution DTS's capability to measure a reliable temperature distribution. On top of this, a numerical examination of the seepage was additionally performed to verify if the predictions of the seepage conditions were valid. To this end, a hydro-thermal coupled numerical analysis was conducted using COMSOL Multiphysics. The analysis consisted of two steps: (1) calibration of the numerical model based on DTS data and reasonable material parameters and (2) verification of the DTS findings based on numerical observations.

5.1 Governing Equations

The mass-balance equation governing the seepage distribution is given by (Bear 2012; COMSOL Multiphysics 2020a; Farthing and Ogden 2017):

$$\left[ns_w C_w + n(1-s_r)\frac{\partial S_e}{\partial p_w}\right]\frac{\partial p_w}{\partial t} = \nabla \cdot \left[k_r \frac{\mathbf{K}_{sat}}{\gamma_w}\nabla(p_w + \rho_w \mathbf{g}\cdot\mathbf{x})\right] \quad (4)$$

where, p_w is the pore-water pressure; n is the porosity; s_w is the degree of saturation; s_r is the residual degree of saturation; S_e is the effective degree of saturation; k_r is the relative permeability function; $\mathbf{K}_{sat}$ is saturated hydraulic conductivity tensor (assumed to be isotropic in this study); ρ_w is the density of water; $\mathbf{g}$ is gravitational acceleration, and $\mathbf{x}$ is the position vector.

For unsaturated conditions, k_r is obtained based on the van Genuchten model as shown below (van Genuchten 1980):

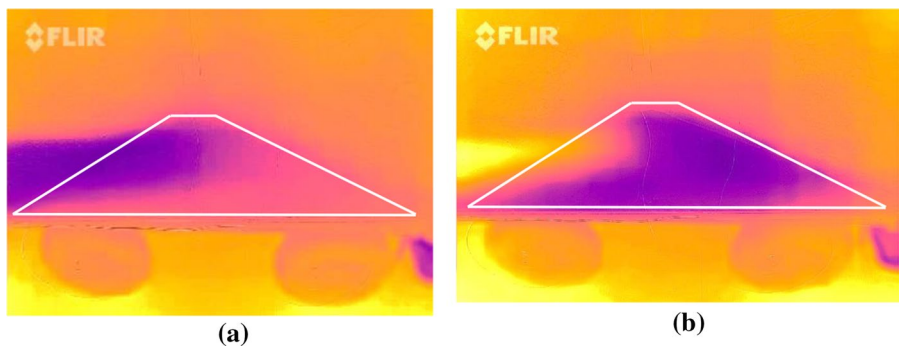

(a) (b)

Fig. 9 Thermal image results; **a** during P-1 (cooling phase), and **b** during P-2 (warming phase)

$$k_r = S_e^{0.5}[1-(1-S_e^{1/m})^m]^2 \quad \text{for} \quad p_w < 0 \tag{5}$$

where, m is a curve-fitting parameter. S_e is be related to negative pore water pressure via the van Genuchten soil–water characteristics curve (SWCC) model (van Genuchten 1980),

$$S_e = \left[1+\left|\alpha_{VG}p_w\right|^{\frac{1}{1-m}}\right]^{-m} \quad \text{for} \quad p_w < 0 \tag{6}$$

where, α_{VG} is a parameter related to air-entry pressure.

The energy-balance equation governing the temperature distribution in the dam is given by (COMSOL Multiphysics 2020b; Ghafoori et al. 2020b; Yosef et al. 2018; Yosef and Song 2015):

$$C_{p,eff}\frac{\partial T}{\partial t} + \rho_w c_{p,w}\mathbf{q}_w \cdot \nabla T = \nabla \cdot (\boldsymbol{\lambda}_{T,eff}\nabla T) \tag{7}$$

where, T is the temperature; $C_{p,eff}$ is the effective heat capacity of the porous media, $c_{p,w}$ is the specific heat capacity of water; $\mathbf{q}_w$ is Darcy's velocity, and $\boldsymbol{\lambda}_{T,eff}$ is effective thermal conductivity tensor (assumed to be isotropic) of the media. The effect of dispersion and heat source/sink terms were ignored. The effective thermal properties of the sand were predicted using mixture models, as shown below,

$$C_{p,eff} = (1-n)\rho_s c_{p,s} + n\rho_w c_{p,w} \tag{8}$$

$$\lambda_{T,eff} = \lambda_{T,s}^{1-n}\lambda_{T,w}^{ns_w} \tag{9}$$

where, $c_{p,s}$ is the specific heat capacity of solid sand; $\lambda_{T,s}$ is the thermal conductivity of solid sand; $k_{T,w}$ is the thermal conductivity of water; ρ_s is the density of solids, and ρ_w is the density of water.

5.2 Domain, Boundary/Initial Conditions, and Mesh

A 3D numerical simulation was performed to account for the influence of the PVC pipes on the seepage. The space occupied by the vertical DTSs was simulated as an opening through the dam. Figure 10 shows the corresponding 3D model geometry and boundary conditions.

The reservoir temperature and pressure head were applied in BC1. In BC2, the seepage was assumed zero while the heat interaction between the surface of the model and the room in boundary was modeled assuming unforced convective heat flux as shown in Eq. (10) (Nield and Bejan 2017),

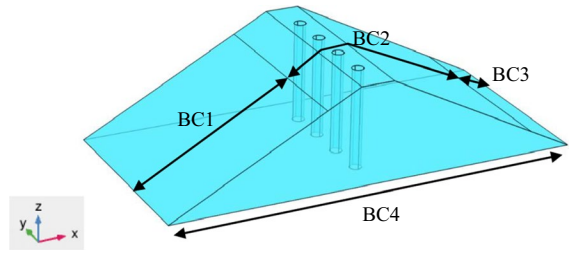

Fig. 10 The numerical model domain and boundary conditions *Note*: BC = Boundary Condition

$$q_h = h(T_{room} - T_{dam}) \tag{10}$$

where q_h is the boundary heat flux; h is the heat transfer coefficient that depends on the geometry of the surface and the behavior of fluid (Incropera et al. 2007); T_{room} is the room temperature, and T_{dam} is the boundary temperature. A typical value for h used in this model is shown in Table 1. In BC3, a seepage face was assumed. The heat flux across this boundary was considered zero, i.e., no heat exchange with the surrounding. BC4 was considered as thermal insulator and impervious. Finally, the initial temperature condition for the transient simulation was inferred from thermometer readings obtained before the beginning of the experiment and was assigned in the numerical modeling.

Tetrahedral elements were used for meshing the model. The mesh sizes were carefully selected based on the Peclet number (Huysmans and Dassargues 2005; Ray et al. 2019). This dimensionless number should be kept low for a numerical stability (usually below 2) by reducing the adopted mesh size or/and flow speed. In this study, the maximum mesh size is assigned as 0.04 m which was small enough to ensure a low Peclet number without imposing high computational cost.

5.3 Material Parameters and Calibration

Due to uncertainty, the material parameters relevant to the problem were computed from a calibration analysis. Three isotropic K_{sat} values were assumed by including the laboratory-determined $K_{sat} = 3.4 \times 10^{-4}$ m/s within the range, as shown in Table 1. The unsaturated soil parameters for sands were assumed from typical values obtained from the literature, as shown in Table 1.

Table 1 Material parameters and their respective values

Material parameter	Value	Unit
Density of solids,ρ_s	2650	kg/m^3
Porosity,n	0.33	Dimensionless
Isotropic hydraulic conductivity,K_{sat}	1×10^{-4},3×10^{-4},5×10^{-4} (best-fit was 2.7×10^{-4})	m/s
[a]Curve fitting parameter,m	0.68	Dimensionless
[a]Curve fitting parameter,α_{VG}	0.035	1/cm
[b]Specific heat capacity of solids,$c_{p,s}$	500, 700, 900 (best-fit was 850)	J/(kg. K)
[c]Thermal conductivity of solids,$\lambda_{T,s}$	2.5, 5.5, 8.5 (best-fit was 5.5)	W/(m. K)
[d]Heat transfer coefficient,h	13.75	W/(m^2. K)

[a]Tuller et al. (2004)

[b]Hamdhan and Clarke (2010);Dong et al. (2015b)

[c]Hamdhan and Clarke (2010); Côté and Konrad (2005); Dong et al. (2015b);Zhang et al. (2015b)

[d]Kosky et al. (2013)

The thermal properties of water were obtained from the built-in material library in COMSOL. Three thermal conductivity and heat capacities of sand were considered from a reasonable range of values in the literature (Côté and Konrad 2005; Dong et al. 2015a; Hamdhan and Clarke 2010; Zhang et al. 2015a), as shown in Table 1. The thermal properties of the PVC and fiber optic cable were not incorporated in this study.

Based on the range of parametric values, a factorial design was prepared. The parametric cases are symbolically designated, for example, K1-CP1-TC1 to refer to the condition when $K_{sat}=1\times10^{-4}$ m/s, $c_{p,s}=500$ J/kgK, and $\lambda_{T,s}=2.5$ W/mK. Then, DTS data were compared with the respective numerical output at three elevations, 18 cm, 12 cm, 6 cm. The best combination was determined as the one that provides the minimum average error for the three locations, as shown below,

$$E_m=\frac{1}{3}\sum_{i=1}^{3}\sqrt{\sum_{j=1}^{k}(T_{DTS,ij}-T_{num,ij})^2} \tag{11}$$

where, E_m is the error measure; $T_{DTS,ij}$ is the temperature from DTS at the ith elevation and jth time index; $T_{num,ij}$ is the temperature output at the same location and time index, and k is the total number of time indices.

Figure 11a shows E_m for the various parametric cases. The best-fitting condition was observed for case K2-CP3-TC2 with $E_m=4.45$. This case was more refined around the best-fitting condition to check if the error could be further reduced. The final improved fit was obtained when $K_{sat}=2.7\times10^{-4}$ m/s, $c_{p,s}=850$ J/(kg. K), and $\lambda_{T,s}=5.5$ W/(m. K) with $E_m=3.80$. As it can be observed, the calibrated K_{sat} was slightly lower than the experimentally estimated $K_{sat}=3.4\times10^{-4}$ m/s. Figure 11b compares numerical and DTS findings using the best parameters showing good match between them.

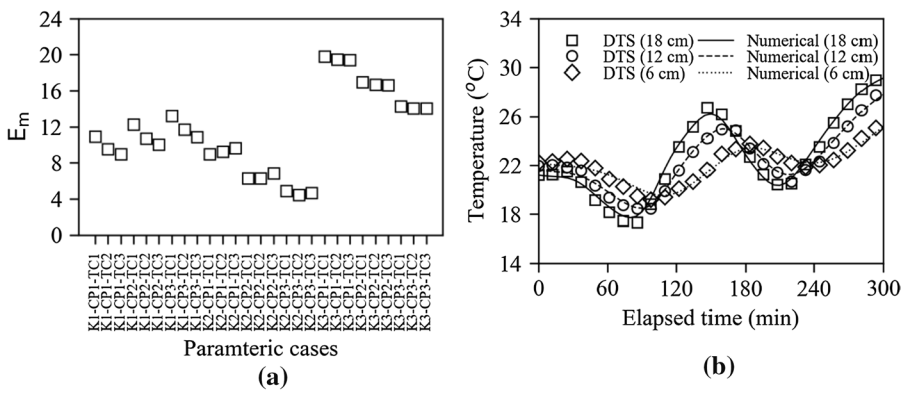

Fig. 11 **a** E_m for various parametric cases, and **b** comparison between numerical and DTS output for the case with the best fit (K2-CP3-TC2)

5.4 5.4 Numerical Results

5.4.1 Temperature Distribution

Figure 12 shows the temperature distribution of the dam at two selected times from P-1 and P-2. Although a constant heat source is applied on the boundary surface, the temperature contour showed a preferential temperature propagation in higher elevations in both phases. But due to the higher temperature difference between dam and room temperature in P-2, the temperature contour can be seen to bend around the phreatic line in P-2 than P-1. This observation from the numerical model generally agreed with the previously discussed laboratory DTS outputs and thermal images.

5.4.2 Phreatic Line

Figure 13 depicts the location of the phreatic line (horizontal dashed line) based on the numerical pore water pressure profile at the dam's center. The temperature distribution (from the warming phase) is also superimposed. Accordingly, the numerical result showed the phreatic line was located at 19.5 cm. This finding agreed with the DTS predicted location, i.e., 19 cm.

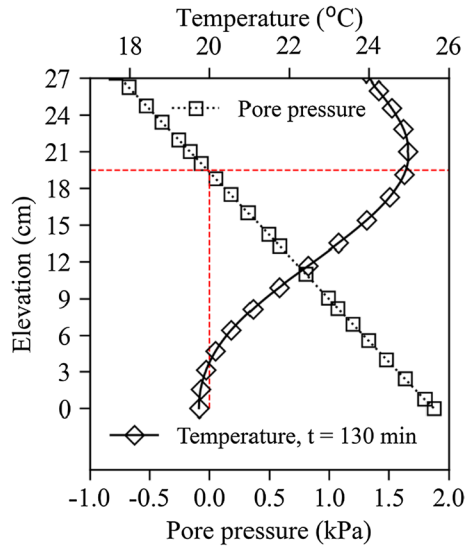

Fig. 13 Pore pressure and temperature distribution at the dam's center

In the same figure, the numerical result showed thermal inflection around the phreatic line. This observation was in line with the previously observed DTS profile that was used to anticipate the location of the phreatic line, in Fig. 7. Thus, it can be concluded that the DTS being able to show the localized temperature curvature around the phreatic line

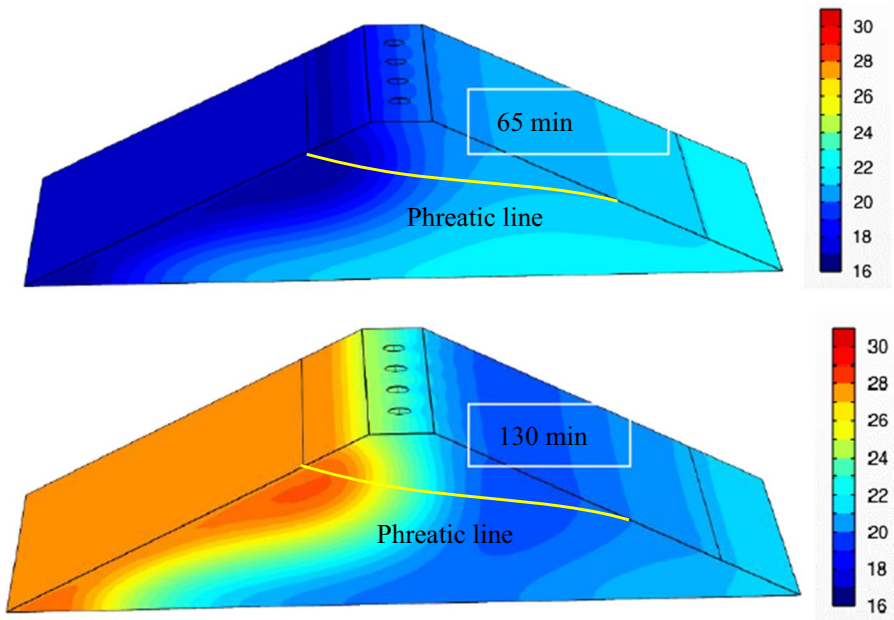

Fig. 12 Temperature distribution at time = 65 min and time = 130 min *Note*: contour units are in °C

demonstrated that it could capture the dam's seepage patterns precisely.

From a practical point of view, the question that may be raised is the application of this approach in identifying phreatic line of field-scale dams. Indeed, research has shown that the phreatic line of dams can be predicted from vertical temperature profiles (Yosef and Song 2015). However, in the absence of considerable thermal propagation to the dam's interior, it may be suggested to employ a heat-up technique (Artières et al. 2007; Aufleger et al. 2008; de Vries et al. 2012). The DTS can be coupled with wires that can be heated up by electrical power. Then, by monitoring the heat dissipation contrast, below and above the phreatic line, the location of the phreatic line may be identified.

5.4.3 Steady-State Seepage Speed

The numerically computed Darcy's seepage speed distribution was evaluated to verify if the DTS reliably described the potential seepage pattern of the dam. To this end, the numerically calculated seepage distribution along the center of the dam is shown in Fig. 14. The contour showed two specific areas of seepage concentrations. These are (1) the location where the phreatic line meets the upstream water and (2) where the water exits the dam downstream (both more than 10×10^{-5} m/s). Additionally, a locally distinct seepage flow speed of 4.5×10^{-5} m/s is observed up to the location of the phreatic line at the dam's center (induced by the PVC pipes). The bottom of the dam on the upstream side exhibited a lower flow speed (less than 2.5×10^{-5} m/s).

Based on DTS data, it was previously stated that there might be higher seepage conditions around higher elevations of the dam. The numerically computed seepage concentration in the area (1) and slow seepage conditions at the bottom of the dam on the upstream side confirmed the validity of that claim. Furthermore, seepage profiles at two elevations (L1, 20 cm and L2, 12 cm), shown in Fig. 14, were plotted and evaluated to understand this behavior more. Figure 15 shows the extracted seepage speed profiles at L1 and L2.

The profiles depicted in the figure showed a seepage contrast in L1 and L2. An area of localized high seepage, with a speed of 7×10^{-5} m/s, is noticed about 14 cm away from the location of the DTS in L1. In L2, the seepage speed is generally lower than L1. Thus, the quick temperature response at higher elevations could be perhaps due to a high seepage that propagated the heat faster due to advection. In addition, the shorter heat travel distance, 19 cm in L1 compared to 35 cm in L2, as shown in Fig. 15, may have contributed to the quick temperature response at the higher positions of the DTS.

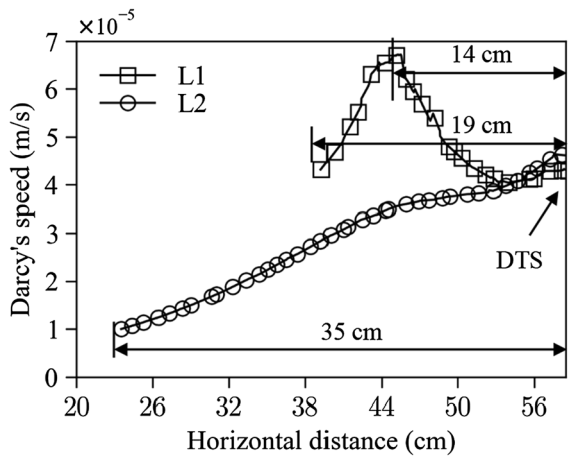

Fig. 15 Darcy's seepage profile along the lines L1 and L2

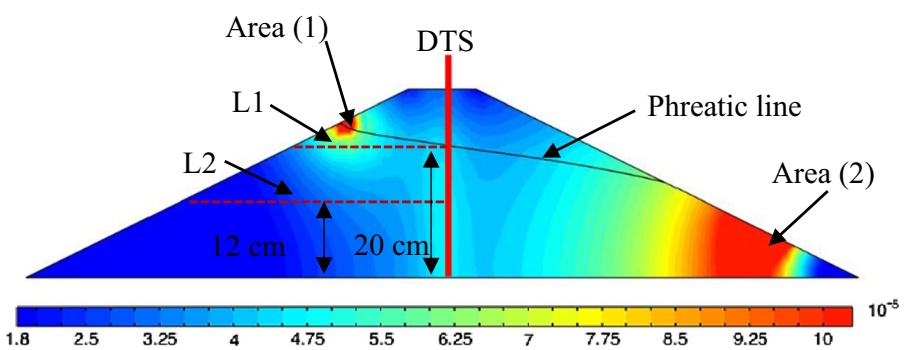

Fig. 14 Darcy's seepage speed distribution in the dam. *Note*: contour unit is m/s

In Fig. 15, notably, an equal seepage speed was noticed near the DTS (dam's center) in L1 and L2. However, the DTS results have shown a temperature contrast with elevation at the dam's center. This result implied that temperature data may not necessarily convey information about the seepage condition at the measurement location. Instead, it may indicate the general seepage conditions upstream of the measurement location, as there was a difference in seepage condition between L1 and L2 upstream of the dam center (where DTSs were installed).

5.4.4 Influence of the PVC Pipes

Finally, the effect of the PVC can be seen by the development of localized higher seepage near the DTS in Figs. 14 and 15. Examination of the steady-state seepage distribution on a horizontal plane at mid-elevation of the dam revealed the same effect more clearly, as shown in Fig. 16. Low seepage speed was induced around the stagnation points located in the front and backside of the PVC pipes. In contrast, high seepage zones were found on the left/right sides. The PVC pipes constricted the flow width and affected the seepage speed, similar to flow around cylindrical objects (Zdravkovich 1997). This behavior is acknowledged as an inherent drawback of the adopted DTS installation approach.

6 Summary and Conclusions

This study demonstrated and evaluated spirally wound custom-manufactured DTS system's capability to capture detailed temperature data and seepage patterns in a laboratory-scale dam, which may be considered 100 times scaled-down from a typical earth dam. It implemented a wound fiber optic cable around a PVC pipe to improve the inherent spatial resolution from 1 m to 8.5 mm. By subjecting the dam to variable temperature, the spatiotemporal temperature variation, phreatic line, and salient features of hydro-thermal coupling such as lag time and amplitude were investigated based on DTS results. Results from the thermal images verified the DTS's capability to capture the model dam's temperature distribution reliably. A 3D numerical modeling based on the hydro-thermal coupled governing equations also demonstrated the DTS's capability to predict seepage patterns of the dam.

The following main conclusions were made from the study:

- Winding the fiber optic cable around an optimally sized pipe can significantly enhance the spatial resolution of DTS. However, the quality of the fiber optic cable must be checked prior to use to avoid poor DTS performance.
- A DTS with wound fiber optic cable around an optimally-sized circular object (e.g., PVC pipe) and checked for light attenuation may be used to obtain detailed temperature data in small-scale laboratory dams.
- A high-resolution DTS may be used to reliably trace seepage patterns in a small laboratory-scale dam based on the principle of hydro-thermal coupling.
- Vertically installed DTS could potentially identify phreatic line of earth dams.

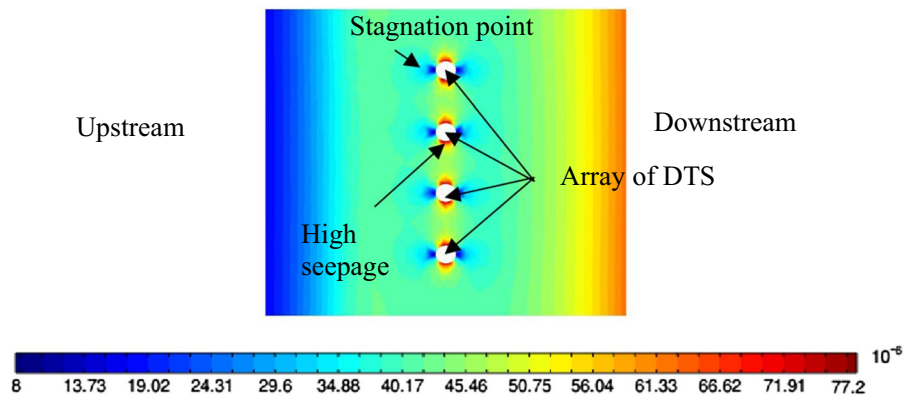

Fig. 16 Seepage distribution at mid-elevation of the dam *Note*: unit is in m/s

- Temperature data collected from DTS may not necessarily reflect the seepage conditions at the measurement location. Instead, it may inform the general seepage condition upstream of the location where DTS is installed.
- The approach presented in this study generally demonstrated that hydro-thermal coupled seepage analysis and DTS could be realistically implemented in a laboratory. The research may promote future research using the same technique and contributes to developing the hydro-thermal coupled method for monitoring seepage through earth dams.

Acknowledgements The authors would like to acknowledge and express appreciation to the Nebraska Department of Transportation (NDOT) for the financial support.

Authors contributions The study conception, funding acquisition, drafting, and editing were by CS. Laboratory testing, data collection, numerical modeling, and the first draft were by BB. Writing review and editing was by JE and SK. All Authors read and approved the final manuscript.

Funding This study was supported by the Nebraska Department of Transportation (NDOT) with research grant 01034D SPR-FY22(004).

Declarations

Conflict of interests The authors have no relevant financial or non-financial interests to disclose.

Data availability All data generated or analyzed during this study are included within the article.

References

ASDSO. 2022. Dam failures and incidents association of state dam safety. Association of state dam safety officials. https://www.damsafety.org/dam-failures. Accessed February 10, 2022.

ASTM International D2434 (2019) Standard test method for permeability of granular soils (Constant Head). ASTM International

ASTM International D2487 (2020) Standard Practice for Classification of Soils for Engineering Purposes (Unified Soil Classification System). ASTM International

Artières O, Bonelli S, Fabre J.-P, Guidoux C, Radzicki K, Royet P and Vedrenne C (2007) Active and passive defences against internal erosion. 235–244

Aufleger M, Goltz M, Perzlmaier S and Dornstädter J (2008) Integral seepage monitoring on embankment dams by DFOT heat pulse method. 9

Bear J (2012) Hydraulics of groundwater. Courier corporation

Belli R, and Inaudi D (2017) Distributed sensors for underground deformation monitoring. 9

Bersan S, Koelewijn AR, Putti M, Simonini P (2019) Large-cale testing of distributed temperature sensing for early detection of piping. J Geotech Geoenviron Eng 145(9):04019052. https://doi.org/10.1061/(ASCE)GT.1943-5606.0002058

Briggs MA, Lautz LK, McKenzie JM, Gordon RP and Hare DK (2012) Using high-resolution distributed temperature sensing to quantify spatial and temporal variability in vertical hyporheic flux. Water Resour Res 48(2):1–16

COMSOL Multiphysics. 2020a. Porous media module, user's guide. COMSOL

COMSOL Multiphysics. 2020b. Heat transfer module, user's guide. COMSOL

Cola S, Girardi V, Bersan S, Simonini P, Schenato L, De Polo F (2021) An optical fiber-based monitoring system to study the seepage flow below the landside toe of a river levee. J Civil Struct Health Monit 11(3):691–705. https://doi.org/10.1007/s13349-021-00475-y

Côté J, Konrad J-M (2005) A generalized thermal conductivity model for soils and construction materials. Can Geotech J 42(2):443–458

Des Tombe B, Schilperoort B, Bakker M (2020) Estimation of temperature and associated uncertainty from fiber-optic raman-spectrum distributed temperature sensing. Sensors 20:2235. https://doi.org/10.3390/s20082235

Dong Y, McCartney JS, Lu N (2015a) Critical review of thermal conductivity models for unsaturated soils. Geotech Geol Eng 33(2):207–221

Dong Y, McCartney JS, Lu N (2015b) Critical review of thermal conductivity models for unsaturated soils. Geotech Geol Eng 33(2):207–221. https://doi.org/10.1007/s10706-015-9843-2

Dornstädter J (1996) Sensitive monitoring of embankment dams. In: Johansson S, Cederstrom M (eds) Repair and upgrading of dams. SwedCOLD, Stockholm, Sweden, pp 1400–1306

Dornstädter J, Fabritius A and Heinemann B (2017) Online alarming for internal erosion. European working group on internal erosion in embankment dams & their foundations, 160

Dornstädter J (2013) Leakage detection in dams—state of the art. 20th SLOCOLD, Ljubljana, 77–86111

FEMA. 2015. Evaluation and monitoring of seepage and internal erosion. Federal emergency management agency, interagency committee on dam safety (ICODS) Washington, D.C

Fabritius A, Heinemann B, Dornstädter J, and Trick T (2017) Distributed fiber optic temperature measurement for dam safety monitoring: current state of the art and further development. Centurion, Tshwane, South Africa

Farthing MW, Ogden FL (2017) Numerical solution of Richards' equation: a review of advances and challenges. Soil Sci Soc Am J 81(6):1257–1269 (**Wiley Online Library**)

Fell R, Fry J-J (2007) Internal erosion of dams and their foundations. CRC Press, Aussois, France

Fell R, Wan CF, Cyganiewicz J, Foster M (2003) Time for development of internal erosion and

piping in embankment dams. J Geotech Geoenviron Eng 129(4):307–314. https://doi.org/10.1061/(ASCE)1090-0241(2003)129:4(307)
Foster M, Fell R, Spannagle M (2000) The statistics of embankment dam failures and accidents. Can Geotech J 37(5):1000–1024
Fry J (2016) Lessons on internal erosion in embankment dams from failures and physical models. Scour and erosion. CRC Press, Oxford U.K, pp 41–58
Garner SJ, Fannin RJ (2010) Understanding internal erosion: a decade of research following a sinkhole event. Int J Hydropower Dams 17:93–98
van Genuchten MT (1980) A closed-form equation for predicting the hydraulic conductivity of unsaturated soils. Soil Sci Soc Am J 44(5):892–898
Ghafoori Y, Maček M, Vidmar A, Říha J, Kryžanowski A (2020a) Analysis of seepage in a laboratory scaled model using passive optical fiber distributed temperature sensor. Water 12(2):367. https://doi.org/10.3390/w12020367
Ghafoori Y, Vidmar A, Říha J, Kryžanowski A (2020b) A review of measurement calibration and interpretation for seepage monitoring by optical fiber distributed temperature sensors. Sensors 20(19):5696
Glisic B, Inaudi D (2008) Fibre optic methods for structural health monitoring. John Wiley & Sons, Ltd
Goltz M (2011) A contribution of monitoring of embankment dams by means of distributed fiber optic measurements. Dissertation
Hamdhan IN and Clarke BG (2010) Determination of thermal conductivity of coarse and fine sand soils. Proceedings of world geothermal congress, 1–7.
Hartog AH (2017) An introduction to distributed optical fibre sensors. CRC Press
Huysmans M, Dassargues A (2005) Review of the use of Péclet numbers to determine the relative importance of advection and diffusion in low permeability environments. Hydrogeol J 13(5):895–904. https://doi.org/10.1007/s10040-004-0387-4
Inaudi D, Glisic B (2007) Distributed fiber optic sensors: novel tools for the monitoring of large structures. Geotech News 25(3):31–35
Incropera FP, Dewitt DP, Bergman TL, Lavine AS (2007) Fundamentals of heat and mass transfer. John Wiley & Sons, Hoboken, NJ
Johansson S (1997) Seepage monitoring in embankment dams. PhD Thesis. Institutionen för anläggning och miljö
Kosky P, Balmer R, Keat W, Wise G (2013) Exploring engineering. Academic Press, Boston, MA, USA
Loupos K, Amditis A (2017) Structural health monitoring fiber optic sensors. In: Matias IR, Ikezawa S, Corres J (eds) Fiber optic sensors: current status and future possibilities, smart sensors, measurement and instrumentation. Springer International Publishing, Cham, pp 185–206
Mattsson H, Hellstrom JGI and Lundstrom TS (2008) On internal erosion in embankment dams : a literature survey of the phenomenon and the prospect to model it numerically. Lulea University of Technology, 70.
Maughan SM, Kee HH, Newson TP (2001) Simultaneous distributed fibre temperature and strain sensor using microwave coherent detection of spontaneous Brillouin backscatter. Meas Sci Technol 12(7):834–842. https://doi.org/10.1088/0957-0233/12/7/315
Nield DA and Bejan A (2017) Convection in porous media, 982
Ray S, Mondal D, Reuveni S (2019) Péclet number governs transition to acceleratory restart in drift-diffusion. J Phys A Math Theor 52(25):255002
Robbins BA and Griffiths DV (2018) Internal erosion of embankments: a review and appraisal. Rocky mountain geo-conference 2018. American Society of Civil Engineers Reston, VA, 61–75
Sarabia A, Meza F, Suárez F (2018) Use of fiber-optic distributed temperature sensing to investigate erosion of the non-convective zone in salt-gradient solar ponds. Sol Energy 170:499–509
Soga K, Ewais A, Fern J, Park J (2019) Advances in geotechnical sensors and monitoring. In: Lu N, Mitchell JK (eds) Geotechnical fundamentals for addressing new world challenges springer series in geomechanics and geoengineering. Springer International Publishing, Cham, pp 29–65
Soga K, Kwan V, Pelecanos L, Rui Y, Schwamb T, Seo H, and Wilcock M (2015) The role of distributed sensing in understanding the engineering performance of geotechnical structures
Song CR, Yosef TY (2017) "Seepage monitoring of an embankment dam based on hydro-thermal coupled analysis. J Eng Mater Technol Trans ASME 139(2):021024. https://doi.org/10.1115/1.4036020
Suárez F, Aravena JE, Hausner MB, Childress AE, Tyler SW (2011) Assessment of a vertical high-resolution distributed-temperature-sensing system in a shallow thermohaline environment. Hydrol Earth Syst Sci 15(3):1081–1093
Torres RL (2009) Considerations for detection of internal erosion in embankment dams. GEO-velopment: The role of geological and geotechnical engineering in new and redevelopment projects, 82–98
Tuller M, Or D, Hillel D (2004) Retention of water in soil and the soil water characteristic curve. Encycl Soils Environ 4:278–289
USBR (2014) Design standard no. 13, embankment dams. U.S. Department of Interior, Bureau of Reclamation
Vries de G, Koelewijn AR and Hopman V (2012) IJkdijk full scale underseepage erosion (piping) test: evaluation of innovative sensor technology. American society of civil engineers. 649–657, https://doi.org/10.1061/41147(392)63
Wu R, Martin V, McKenzie J, Broda S, Bussière B, Aubertin M, Kurylyk BL (2020) Laboratory-scale assessment of a capillary barrier using fibre optic distributed temperature sensing (FO-DTS). Can Geotech J 57(1):115–126
Xiao H, Huang J (2013) Experimental study of the applications of fiber optic distributed temperature sensors in detecting seepage in soils. Geotech Test J 36(3):360–368
Yosef TY, Song CR, Chang K-T (2018) Hydro-thermal coupled analysis for health monitoring of embankment dams. Acta Geotech 13(2):447–4554
Yosef TY and Song CR (2015) Seepage-heat coupled analysis for estimating phreatic line of an earth dam from temperature profile. Symposium on the application of geophysics to engineering and environmental problems 2015, Society

of exploration geophysicists and environment and engineering, 252–256
Zdravkovich MM (1997) Flow around circular cylinders: volume2: applications. Oxford University Press
Zhang N, Yu X, Pradhan A, Puppala AJ (2015a) Thermal conductivity of quartz sands by thermo-time domain reflectometry probe and model prediction. J Mater Civil Eng 27(12):04015059
Zhang N, Yu X, Pradhan A, Puppala AJ (2015b) Thermal conductivity of quartz sands by thermo-time domain reflectometry probe and model prediction. J Mater Civ Eng 27(12):04015059. https://doi.org/10.1061/(ASCE)MT.1943-5533.0001332